Feature Preserving Non-Rigid Iterative Weighted Closest Point and Semi-Curvature Registration

Farzam Tajdari, Toon Huysmans, Yusheng Yang, and Yu Song, *Member, IEEE*

Abstract—Preserving features of a surface as characteristic local shape properties captured e.g. by curvature, during non-rigid registration is always difficult where finding meaningful correspondences, assuring the robustness and the convergence of the algorithm while maintaining the quality of mesh are often challenges due to the high degrees of freedom and the sensitivity to features of the source surface. In this paper, we present a non-rigid registration method utilizing a newly defined semi-curvature, which is inspired by the definition of the Gaussian curvature. In the procedure of establishing the correspondences, for each point on the source surface, a corresponding point on the target surface is selected using a dynamic weighted criterion defined on the distance and the semi-curvature. We reformulate the cost function as a combination of the semi-curvature, the stiffness, and the distance terms, and ensure to penalize errors of both the distance and the semi-curvature terms in a guaranteed stable region. For a robust and efficient optimization process, we linearize the semi-curvature term, where the region of attraction is defined and the stability of the approach is proven. Experimental results show that features of the local areas on the original surface with higher curvature values are better preserved in comparison with the conventional methods. In comparison with the other methods, this leads to, on average, 75%, 8% and 82% improvement in terms of quality of correspondences selection, quality of surface after registration, and time spent of the convergence process respectively, mainly due to that the semi-curvature term logically increases the constraints and dependency of each point on the neighboring vertices based on the point's degree of curvature.

Index Terms—Non-rigid registration, curvature, non-linearity, region of attraction.

I. INTRODUCTION

IN THE past decade, non-rigid registration is widely applied in many applications such as motion analysis [1], shape analysis [2], and medical image registration [3]. Among different types of non-rigid surface registration methods, the non-rigid Iterative Closest Point (ICP) registration attracted much attention, mainly due to its simplicity, efficiency and effectiveness [4]. Using the non-rigid ICP method, a source surface is registered to the target surface via two iterative steps. First, the correspondence of each vertex in the source surface to the target surface is established based on a metric, which usually is defined as a type of distance (e.g. distance between points). Then, a cost function is defined based on those correspondences, and is minimized by finding a nonrigid transformation [5]. In a practical application, these two steps iterate until a local minimum of the cost function is found or the iteration steps exceed a threshold.

Though it was successfully applied in many applications, e.g. gender scoring [6], statistical shape modeling [7], computer vision [8], multimedia applications [9], human-computer interactions [10], 3D deformation of the human spinal column detection [11], image face alignment [12], and 3D human body analysis [13], the non-rigid registration is a non-trivial and ill-defined problem with a high number of degrees-of-freedom (DOFs). Accordingly, there are many challenges for preserving features of the source surface in the design and implementation of a non-rigid ICP registration algorithm [14]. Here features account for salient geometric features which form compound higher-level descriptors. A salient geometric feature, or in short, a salient feature, consists of a cluster of descriptors that locally describe a nontrivial region of the surface [15] i.e. curvature. Those challenges are, e.g. establishing meaningful robust correspondences in each step of the iteration [16], ensuring the convergence towards the desired minimum in the optimization [17], and maintaining the quality of the mesh regarding the source surface. A typical example is that in the minimization of distances between closest points from the target to the source surfaces, the correspondences between feature points may change when the stiffness term, or the weight of it, is not large enough. This is especially true when the feature is not prominent, or when there is interference between/among features.

In the past decades, researchers made considerable progress in tackling those challenges, for instance, using landmarks (LMs) to improve the accuracy of the correspondences [18]–[21], introducing prior knowledge regarding the geometric shapes [22], integrating more terms in the cost functions [23]. However, problems are not fully solved. For instance, in matching 3D scans of human feet, it is often

found that some toes are bonded together and/or part of a toe is hidden behind another. Though researchers tried to introduce LMs, either manually or automatically, the limited number of LMs does not always contribute to establishing the desired correspondences between source and target surfaces, neither lead to a correct registration result. A better measure, which synthesizes the intrinsic properties of features of both the source and the target surface, is needed in establishing the meaningful correspondences as well as defining the cost function.

In this paper, we propose a new asymptotically robust approach of non-rigid ICP by integrating a newly defined semi-curvature in the definition of the metric for establishing the correspondences as well as the cost function for finding the non-rigid transformation. Our scientific contributions are:

1. We introduce the semi-curvature, which is monotonically related to the Gaussian curvature with similar geometric meaning, and has unique mathematical characteristics of the capability of being linearized;
2. We integrate the semi-curvature in the cost function for establishing corresponding point pairs in two surfaces using a dynamic weighting factor to address intrinsic properties across the complete surfaces;
3. We linearize the cost function with guaranteed regions of attraction in the minimization process for a robust registration process as well as a registration result with high quality mesh.

The remainder of the paper is arranged as follows: first recent developments in the non-rigid ICP registration method regarding the aforementioned three challenges are presented. Then we propose our approach where the definition and the characteristics of the semi-curvature are addressed. In Section IV, the setup of the experiments is introduced where in Section V, experimental results on the comparison of the proposed approach and other non-rigid registration methods are presented. Finally, a short conclusion is drawn and future research directions are highlighted as well.

II. RELATED WORK

A. Correspondences

For a better preservation of the features on the source surface, establishing meaningful dense correspondences between the source and the target surface throughout the registration process is key. Using LMs is a common method to improve the accuracy of the correspondences in the registration process. Besides manual specification of corresponding points on the two surfaces, pattern recognition algorithms are often deployed to find those LMs automatically, e.g. [18]–[21]. However, those LMs are often located at the extrema of certain intrinsic properties and they are sparsely distributed around the surface. The full spectrum of the intrinsic properties of the surface is often not completely used in the process of establishing correspondences. To embed more shape information in the registration process, researchers introduced different intrinsic properties in establishing the correspondence. For instance, Li [24] employed a single ℓ_2-norm optimization framework utilizing confidence weights to improve

robustness. Dai *et al.* [25] presented an iterative registration method that combines ICP with Coherent Point Drift (CPD) to achieve a more stable correspondence establishment. As a recent improvement, a Bayesian Coherent Point Drift (BCPD) approach was presented in [26]. The method utilizes the coherent drift in the variational Bayesian inference theory, while keeping the fundamental features of the CPD algorithm. Recently, a rigid ICP based registration algorithm was presented in [27] which uses curvature feature similarity to find more accurate correspondences. However, the method is sensitive to noise, and the exponential growth of the computing time regarding the number of points in the surfaces also prevents its wide application to more complicated geometries. Besides shape intrinsic properties, prior knowledge can also contribute to establish meaningful correspondence. For instance, Hontani *et al.* [22] used a reference statistical shape model (SSM) to find outliers in the non-rigid registration. Guo *et al.* [28] proposed an ℓ_0 model for establishing correspondences between deformed body shapes, and this method had higher accuracy and robustness in dynamic 3D reconstruction and tracking. However, the construction of an SSM [29] is always an expensive task regarding both the manpower and the computing time, and it is not always possible to build an SSM a priori regarding the shape to be registered.

B. Convergence in the Minimization

With meaningful correspondences between the source and the target surfaces, a robust minimization strategy that is used in each step of the registration is essential for a successful registration. A few works addressed this issue regrading the metrics in the cost function, the initial conditions and the non-rigid transformation. For instance, Sharp *et al.* [30] used the Euclidean and topological metrics to reduce the probability of instability and possible deviation from the global minimum. The effect of initial condition was investigated in [31], where a better initial condition was proposed using a novel evaluation method based on the genetic algorithm. Regarding the rigid transformation, the transformation of the surface was restricted to the rotation with the normal vector of the faces in [32] to guarantee the robustness only for rotation components. To extend the domain of robustness (following global robustness) of the rotation angles, constraints of the rotations are proposed in [33] to limit the unnecessary rotational transformation that leads to instability. Recently, Uttaran *et al.* [34] presented a fast and locally robust SE-based (Special Euclidean) methodology that optimizes a cost function based on motion estimation [35]. Haris *et al.* [36] introduced the local minimum escape ICP algorithm, improving the conventional ICP method by proposing local minimum estimation and escape mechanisms. However, the robustness of the minimization strategy was not yet fully guaranteed.

C. Mesh Quality

Preserving mesh quality can be attributed to part of the feature preservation in a local scale, e.g. details of the shape intrinsic properties might be lost if the resulting surface of

the non-rigid registration is too smooth. Knupp [37] indicated that the mesh quality can be quantified as "*an element quality metric is a scalar function of node positions that measures some geometric property of the element*". Therefore, to preserve the mesh quality of the surface after registration, embedding regularization terms, e.g. ℓ_2-norm in a least-squares sense [38], in the formulation of the cost function is a popular choice. For instance, Amberg *et al.* [39] introduced an ℓ_2-norm cost function where a stiffness term is embedded to have more logical deformation considering the similarity of the surfaces. Sumner *et al.* [40] employed the as-rigid-as-possible term introduced by [41] to the cost function. In 2009, Liao *et al.* [42] described a Thin Plate Spline (TPS) based terms [43], and combined it with graduated assignment algorithm to formulate smoothness constraints. Rouhani *et al.* [44] also integrated locally rigid transformations to formulate the non-rigid deformation optimization problem. A sparse non-rigid registration method using an ℓ_1-norm cost function is employed by Yang *et al.* [45]. However, the position constraints (e.g. near piece-wise rigid deformation) were not sufficiently well embedded in the model to establish the connectivity of the piece-wise rigid deformation. Li *et al.* [17] recruited local affine transformations and orthogonality constraint together to capture surface details for preserving local shape in the registration [46], [47]. Different densities in the source and the target meshes also pose challenges to preserving mesh quality in the non-rigid registration. For a better match of similar surfaces in the source and target surfaces with different point densities, Tazir *et al.* [48] proposed the idea of matching points representing the local regions of the source cloud with the points representing the corresponding local regions in the target. Recently, Ayan [49] presented a registration method based on an energy function combining the strength of local and global geometry along with an intermediate level representation of the point cloud. The method is practical to address uniform deformation and preserve the original mesh quality; however, it is very sensitive to the point density, high deformation and detailed geometry areas.

III. METHODOLOGY

This section introduces the proposed non-rigid ICP approach. First, a concise description of the approach is given based on the conventional ICP algorithm [39]. This is followed by the introduction of the semi-curvature term, the improved corresponding points search approach, the cost function and the optimization process.

A. The Approach

In the registration process of the non-rigid ICP, the source surface $\mathcal{S} = (\mathcal{V}, \mathcal{E})$, consisting of n vertices in $\mathcal{V}$ and m edges in $\mathcal{E}$, is registered to the target surface $\mathcal{T}$ step by step. Fig. 1 illustrates a step of the registration process. In the figure, the meshes are assumed to be triangular meshes, and the vertices are labeled by numbers. In this step, first, the correspondences between vertices v_i in the source surface $\mathcal{S}$ (green) and vertices u_i in the target surface $\mathcal{T}$ (red) are established. Then v_i is
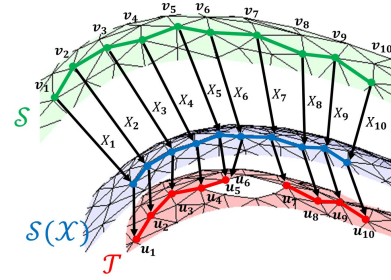

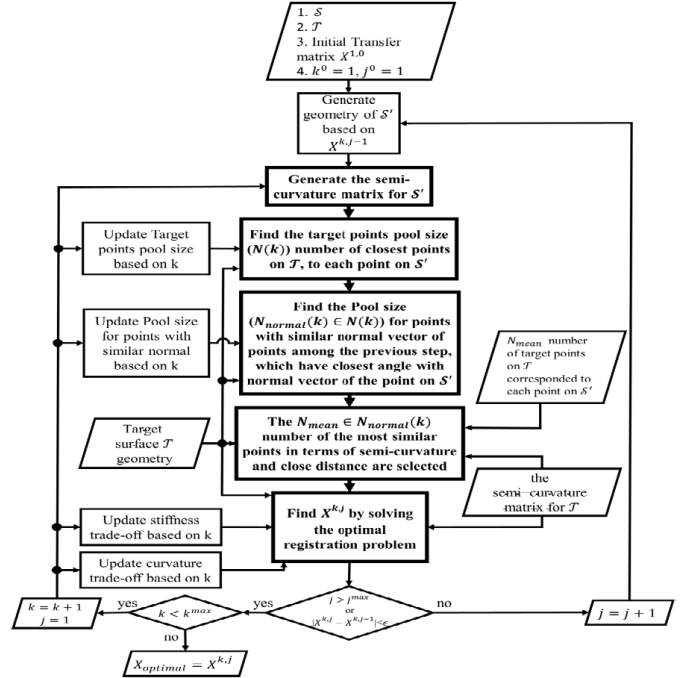Fig. 1. Match the source surface to the target surface.

Fig. 2. The proposed registration process.

transformed by locally affine transformations (X_i) towards the target surface $\mathcal{T}$ (red). The transformed source surface is $\mathcal{S}(X)$ (blue). This procedure iterates till an optimal stable state is obtained.

Based on the basic concept introduced in Fig. 1, the flowchart in Fig. 2 describes the proposed iterative approach by finding optimal X_i to transform v_i to u_i (where u_i is comparable with $X_i v_i$) in each iteration. It is worth mentioning that in the approach of Fig. 2 there are two nested loops. In the outer loop (where k is updated), the weights in the metric for establishing correspondences are automatically updated. In the inner loop (where j is updated), the cost function for finding the optimal transformation matrix is continuously being minimized based on the weights till the change in X is less than a small value of ϵ or $j > j^{\max}$. The two nested loops in each of their iterations account for addressing different aspects of the measures, e.g. the Euclidean distance and the difference of semi-curvatures of two corresponding points.

As a final step in the registration, each vertex of $\mathcal{V}(X)$ is projected onto the target surface along the normal vectors of the transformed surface. Keeping the original topology of
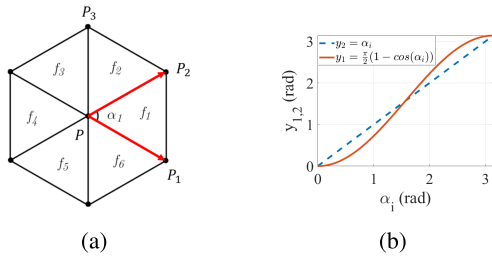
Fig. 3. (a) Curvature parameters of point P. (b) Relations between α_i and $\frac{\pi}{2}(1 - cos(\alpha_i))$.

Fig. 4. Visualisation of normalised curvature values. (a) Using Gaussian curvature. (b) Using the proposed semi-curvature.

the source mesh, the final transformed vertices represent the registered surface of the original source.

B. Semi-Curvature

Using the notation from Fig. 3(a), the Gaussian curvature of a point P on a triangular mesh can be approximated [50] as:

$$K_G(P) = \frac{3\left(2\pi - \sum \alpha_i\right)}{\sum \mathcal{A}(f_i)} \quad (1)$$

where, α_i is the angle of the triangle formed by P and its 1-ring neighboring vertices. It can be calculated as Eq. (2).

$$\alpha_i = cos^{-1}\left(\frac{\left(\overrightarrow{P}_i - \overrightarrow{P}\right) \cdot \left(\overrightarrow{P}_{i+1} - \overrightarrow{P}\right)}{\left\|\overrightarrow{P}_i - \overrightarrow{P}\right\| \left\|\overrightarrow{P}_{i+1} - \overrightarrow{P}\right\|}\right) \quad (2)$$

$\mathcal{A}$ in Eq. (1) is a function to calculate the area of each triangle f_i. It can be approached as:

$$\mathcal{A}(f_i) = 0.5 \left\|\left(\overrightarrow{P}_i - \overrightarrow{P}\right) \times \left(\overrightarrow{P}_{i+1} - \overrightarrow{P}\right)\right\| \quad (3)$$

As the function cos^{-1} in Eq. (2) makes the relationship between Gaussian curvature values and vectors of P to P_i nonlinear, we replace α_i in Eq. (1) by $\frac{\pi}{2}(1 - cos(\alpha_i))$. For a triangle mesh, $0 \leq \alpha_i \leq \pi$, therefore the domains of α_i is the same as $\frac{\pi}{2}(1 - cos(\alpha_i))$ for all vertices. Regarding the values, these two expressions equal to each other at $\alpha_i = 0$, $\frac{\pi}{2}$, and π, however, slightly different in other α_i as y_1 and y_2 is shown in Fig. 3(b). Replacing α_i by $\frac{\pi}{2}(1-cos(\alpha_i))$ in Eq. (1), we define the semi-curvature of vertex P as:

$$K(P) = \frac{3(2\pi - \sum \frac{\pi}{2}(1 - cos(\alpha_i)))}{\sum \mathcal{A}(f_i)} \quad (4)$$

The newly defined semi-curvature in Eq. (4) and the Gaussian curvature suggested by Eq. (1) are monotonically related as Fig. 3(b). For acute α_i, we have $y_1 < y_2$ and when α_i is obtuse, $y_1 > y_2$ holds. According to Eq. (4), if a part of a mesh consists only of acute triangles, the value of semi-curvature on each vertex is larger than Gaussian curvature and for obtuse triangles, the value is smaller. Therefore, compared to the Gaussian curvature, semi-curvature might have a larger value when the valence of the vertex, i.e. the number of one-ring vertices, is large, e.g. $\geq$5. This transformation from the Gaussian curvature Eq. (4) to the semi-curvature Eq. (1), as regulator of curvature, is instigated
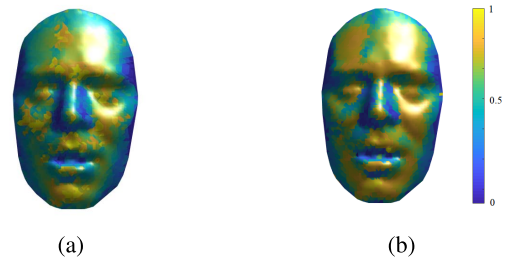
by increasing the chance of visibility of the features (suggested by semi-curvature function versus curvature function on saddle points) as it is found, complex models' features usually are indexed to their saddle points [23]. Thus, enlarging the deviation spectrum between high curved and low curved points can improve corresponding points selection between the two meshes. To clarify, the Gaussian curvature region was further addressed as depicted in Fig. 4. In the figure, it can be observed that using the semi-curvature, the yellow region on the face (Fig. 4(b)) is larger compared to using the Gaussian curvature (Fig. 4(a)). Generally, the saddle points come into view because of exaggeration in the semi-curvature function. It is expected that the function would attempt to keep larger deviation of the semi-curvature value differences to provide a higher chance of detecting the corresponding saddles. This logical deviation gives more freedom to the deformation with less confliction between several correspondences. Moreover, increasing the valence of a vertex results in an increase of the semi-curvature value, the registration will be enhanced to logically exert different stiffness values for the areas with more features. This concludes to have $\mathcal{S}$ with different stiffness in different parts based on the degree of pronouncedness of feature that exists in the area.

Thus, the new curvature formulation satisfies the goal of this paper, to emphasize more on highly curved areas. As an example in Fig. 4, the location of high curved (yellow), and low curved (blue) areas are the same comparing Fig. 4(a) with Fig. 4(b), while the area of the domains is different.

C. Establish Correspondences

In the use of a conventional ICP method, given a point on $\mathcal{S}$, the closest point on $\mathcal{T}$ is considered as its corresponding point. As only the Euclidean distance is used in establishing the correspondences, the intrinsic properties of the surface are not embedded. To avoid the loss of intrinsic properties, we introduce a new criterion as Eq. (5), which combines the Euclidean distance and semi-curvature to find the candidate point on $\mathcal{T}$.

$$H = \zeta^\eta H_d + (1 - \zeta^\eta)H_c \quad (5)$$

where H_d is the distance term composed of h_{d_i} related to P_i, and H_c is the differential semi-curvature term composed of h_{c_i} related to P_i. Moreover, in Eq. (5), ζ is a linearly increasing coefficient by k in range of $[0, 1]$, and η is a

constant parameter. The higher the value over 1 for η, the larger the effect of semi-curvature values is in driving the corresponding points selection by H. Accordingly, the smaller the η is than 1, the lower the effect of semi-curvature values are to select the correspondences by H. In the case that η is equal to 1, both distance (H_d) and semi-curvature (H_c) have equal effect in terms of the H for correspondences selection.

In practice, sparse similarities prevent us to search all points in $\mathcal{T}$ for establishing correspondences. Therefore, we only consider candidate correspondence points in a pre-processed region including N_{normal} number of points in $\mathcal{T}$. Then, H_d and H_c in Eq. (5) can be elaborated as:

$$[h_{c_i}]_{N_{normal} \times 1} = \frac{\frac{K(P_i)}{max(K)} - \frac{[K_{target}]_{N_{normal} \times 1}}{max(K_{target})}}{max \left(\frac{K(P_i)}{max(K)} - \frac{[K_{target}]_{N_{normal} \times 1}}{max(K_{target})} \right)} \quad (6)$$

$$[h_{d_i}]_{N_{normal} \times 1} = \frac{v_i - [U]_{N_{normal} \times 1}}{max \left(v_i - [U]_{N_{normal} \times 1} \right)} \quad (7)$$

where K_{target} consists of the semi-curvature values of the points on the $\mathcal{T}$ and arranged based on correspondences, H_d is a N_{normal} by 1 matrix, consisting of distances of the N_{normal} points from $\mathcal{T}$ to P_i on $\mathcal{S}$, and $U = [u_1 \cdots u_n]^T$. The pre-processing procedure to find the region with N_{normal} points has several steps as follows.

- Briefly, N (lowering value, from $N_r n$ to N_{mean}) number of closest points on $\mathcal{T}$ to each point on $\mathcal{S}$ are chosen, where N_r is a ratio in [0 1] and n is the number of vertices on target surface.
- Then, N_{normal} (lowering value, from M_{normal} to N_{mean}, number of vertices with most similar angle (between normal vector of the vertices on $\mathcal{T}$ and current point on $\mathcal{S}$) are selected.
- Finally, N_{mean} number of the candidate vertices with a lower value of H are picked among the previous step in which the final corresponding point is the average of these N_{mean} vertices.

Once the correspondences are selected from the target, we check the number of aligned vertices from the source to each of the points of the target. For the ones aligned to more than N_{mean} number of source vertices, we only select the N_{mean} of them with minimum H. At the end, for the source vertices that have less than N_{mean} connections, we consider the corresponded point as the transformed point of previous step. This may avoid conflicts between the correspondences and preserve the original mesh detail (shape of the surface's faces).

D. The Cost Function & Minimization

In this section, based on the established correspondences (v_i, u_i), a cost function consisting of different terms is defined and then minimized with guaranteed stability, convergence, and robustness. In the following we introduce each term in the cost function first, then we describe the optimization process based on the linearised cost function.

1) Conventional Terms From Amberg [39]: For a non-rigid registration, the distance of the deformed source and the target should be minimized. Thus, a distance term is selected as the first component of the cost function to be minimised as,

$$E_d = \sum_{v_i \in \mathcal{V}} w_i \|X_i v_i - u_i\|^2, \quad (8)$$

where, w_i is the weight of the distance term, X describes a set of transformations of displaced source vertices $\mathcal{V}(X)$. The transformation matrix X_i for each vertex in the source is a 3×4 transformation matrix as:

$$X_i = \begin{bmatrix} r_{xx} & r_{xy} & r_{xz} & d_x \\ r_{yx} & r_{yy} & r_{yx} & d_y \\ r_{zx} & r_{zy} & r_{zz} & d_z \end{bmatrix}, \quad (9)$$

where r, and d define all afine transformations. The transformation matrix X of all vertices is described in a $4n \times 3$ matrix as $X = [X_1 \cdots X_n]^T$.

A canonical form of Eq. (8) is addressed in Eq. (10), introduced by swapping the position of transformation matrix, and correspondences (v_i, u_i). The sparse matrix D is formed to facilitate the transformation of the source vertices with the individual transformations contained in X via matrix multiplication, and denoted as $D = diag(v_1^T, v_2^T, \ldots, v_n^T)$. The corresponding points are also arranged as $U = [u_1 \cdots u_n]^T$ and the distance term can be derived as:

$$E_d = \|W(DX - U)\|_F^2 \quad (10)$$

where W is a diagonal matrix consisting of weights w_i. To regularise the deformation, an additional stiffness term is employed. Using the Frobenius norm $\|.\|_F$, the stiffness term penalizes difference of the transformations of neighboring vertices, through a weighting matrix $G = diag(1, 1, 1, \gamma)$.

$$E_s = \sum_{i, j \in \mathcal{E}} \left\| (X_i - X_j) G \right\|_F^2 \quad (11)$$

During the deformation, γ is a parameter to stress differences in the skew and rotational part against the translational part of the deformation. The value of γ can be specified based on data units and the types of deformation [39].

Addressing the function of the stiffness term to penalise differences of transformation matrices of the neighboring vertices, the node-arc incidence matrix M (e.g. Dekker [51]) of the template mesh topology is employed to convert the stiffness term functional into a matrix form. As the matrix is fixed for directed graphs, the construction is one row for each edge of the mesh and one column per vertex. To establish the node-arc incidence matrix of the source topology, the indices (i.e. the subscripts) of edges and vertices are addressed, for any edge of r which is connected to vertices (i, j), in r^{th} row of M, and the nonzero entries are $M_{ri} = -1$ and $M_{rj} = 1$. Therefore, we formulate the stiffness term as

$$E_s = \|(M \otimes G) X\|_F^2 \quad (12)$$

2) Semi-Curvature Term: Using distance term only does not fully utilize the intrinsic properties of the surfaces, e.g. high curvature regions were not addressed, this may lead to sub-optimal solutions of the registration. Moreover, it may cause conflicts between different parts of a shape, e.g. selecting the same parts on the target as correspondences for different parts on the source, which are far from the correct corresponding (group of) vertices on the source surface. Thus, considering an extra term, which is independent of the distance term, in the cost function to preserve features is necessary to avoid such problems. In the proposed approach, we embed a new term defined on the semi-curvature to eliminate the conflations, and to address the intrinsic properties across the surface. It contains the differences of semi-curvature values of the points on $\mathcal{S}$ with the correspondences on $\mathcal{T}$ as follows.

$$E_c = \left\| K - K_{target} \right\|_F^2 \qquad (13)$$

To reveal the connection of $K(P)$ in Eq. (4) with X, here we extend $cos(\alpha_i)$ based on the transfer matrix

$$cos(\alpha_i) = \frac{\left(\overrightarrow{P}_i - \overrightarrow{P}\right) \cdot \left(\overrightarrow{P}_{i+1} - \overrightarrow{P}\right)}{\left\|\overrightarrow{P}_i - \overrightarrow{P}\right\| \left\|\overrightarrow{P}_{i+1} - \overrightarrow{P}\right\|}$$

$$= \frac{\left(D_{P_i} - D_p\right) X X^T \left(D_{P_{i+1}} - D_p\right)^T}{\left\|\overrightarrow{P}_i - \overrightarrow{P}\right\| \left\|\overrightarrow{P}_{i+1} - \overrightarrow{P}\right\|} \qquad (14)$$

where we use $D_{P_{i+1}}$, D_{P_i}, and D_P to denote the corresponding row of D to the points P_{i+1}, P_i, and P, respectively. Generally, $D_{P_{i+1}}$ is a $1 \times 4n$ row in D with the same index that P_{i+1} has in $\mathcal{V}$. If we define

$$a_{f_i} = \left[\frac{\left(D_{P_i} - D_p\right)}{\left\|\overrightarrow{P}_i - \overrightarrow{P}\right\| \left\|\overrightarrow{P}_{i+1} - \overrightarrow{P}\right\|} \right]_{1 \times 4n},$$

$$c_{f_i} = \left[\left(D_{P_{i+1}} - D_p\right)^T \right]_{4n \times 1},$$

Eq. (14) turns to be

$$cos(\alpha_i) = \left[a_{f_i}\right]_{1 \times 4n} X_{4n \times 3} X_{3 \times 4n}^T \left[c_{f_i}\right]_{4n \times 1} \qquad (15)$$

Using Eq. (15) to replace the α_i in Eq. (4), the semi-curvature can be calculated as:

$$K(P) = \left(\frac{3\pi}{2} \frac{\sum a_{f_i}}{\sum \mathcal{A}(f_i)}\right) X X^T \left(\sum c_{f_i}\right) - \left(\frac{-6\pi + \frac{3\pi}{2} \sum 1}{\sum \mathcal{A}(f_i)}\right). \qquad (16)$$

Let's consider,

$$\underline{a}_P = \frac{3\pi}{2} \frac{\sum a_{f_i}}{\sum \mathcal{A}(f_i)} \qquad (17)$$

$$\underline{c}_P = \sum c_{f_i} \qquad (18)$$

$$\underline{b}_P = \frac{-6\pi + \frac{3\pi}{2} \sum 1}{\sum \mathcal{A}(f_i)} \qquad (19)$$

The semi-curvature matrix on $\mathcal{S}$ is defined as:

$$K_{n \times n} = \left[\underline{A}_{n \times 4n} X_{4n \times 3} X_{3 \times 4n}^T \underline{C}_{4n \times n}\right]_{n \times n} - \underline{B}_{n \times n} \qquad (20)$$

where $\underline{A} \in \mathbb{R}^{n \times 4n}$, which is a sparse matrix composed of elements $\underline{a}_P$. Similarly, $\underline{C} \in \mathbb{R}^{4n \times n}$, which is a sparse matrix

composed of elements $\underline{c}_P$. $\underline{B} \in \mathbb{R}^{n \times n}$ is a diagonal matrix composed of elements $\underline{b}_P$. Similarly, $K \in \mathbb{R}^{n \times n}$, is a diagonal matrix composed of the semi-curvature values of vertices on S. Thus, to minimize the difference of the semi-curvature between a point on the source and the corresponding point on the target, the semi-curvature term, in the cost function as E_c is presented as follows

$$E_c(X) = \left\| K - K_{target} \right\|_F^2$$

$$= \left\| \underline{A} X X^T \underline{C} - (\underline{B} + K_{target}) \right\|_F^2$$

$$= \left\| \underline{A} X^2 - (\underline{B} + K_{target}) \underline{C}^{-1} \right\|_F^2 \left\| \underline{C} \right\|_F^2 \qquad (21)$$

where, K_{target} consists of the semi-curvature values of vertices on $\mathcal{T}$, calculated through Eq. (4) and arranged based on correspondence points. As $\left\| \underline{C} \right\|_F^2$ is a constant matrix in all iterations, it is considered as part of the weight matrix of W_c, or can be neglected. Also, note that in Eq. (21), $\underline{C}^{-1}$ is the Moore-Penrose pseudoinverse of matrix $\underline{C}$.

E. Linearise E_c

In order to integrate the semi-curvature term in the cost functions for optimization, it is necessary to linearise the semi-curvature term toward the forms of other terms, e.g. Eq. (8). To linearise the semi-curvature term, we assume

$$f(X) = \underline{A} X^2 - (\underline{B} + K_{target}) \underline{C}^{-1}. \qquad (22)$$

If we consider linear format of $f(X)$ as $f_l(X)$, then

$$f_l(X) = A_l X + B_l \left(-(\underline{B} + K_{target}) \underline{C}^{-1}\right). \qquad (23)$$

From [52], A_l, and B_l are

$$A_l = \frac{\partial(\underline{A} X)}{\partial X} = \underline{A}$$

$$B_l = \frac{\partial\left(-(\underline{B} + K_{target}) \underline{C}^{-1}\right)}{\partial\left((\underline{B} + K_{target}) \underline{C}^{-1}\right)} = -1$$

As A_l and B_l are independent to X, the linear system is valid around any point. The final linearised semi-curvature term is

$$f_l(X) = \underline{A} X - \left((\underline{B} + K_{target}) \underline{C}^{-1}\right) \qquad (24)$$

Considering, $E_c(X) = \|f_l(X)\|_F^2$, $A_c = \underline{A}$, and $B_c = (\underline{B} + K_{target}) \underline{C}^{-1}$, the semi-curvature term can be denoted as:

$$E_c(X) = \|W_c (A_c X - B_c)\|_F^2 \qquad (25)$$

1) Stability Analysis: As we linearised the curvature term in Eq. (21), it is possible that X, which minimises $\|A_c X - B_c\|^2$, cannot minimise $\left\| A_c X^2 - B_c \right\|^2$. Thus, here we investigate the impact of $X^o = \frac{A_c^T B_c}{A_c^T A_c}$ on the nonlinear cost function. From Khalil [52], [53], for any system, if $E(X) > 0$ and $\frac{\partial E}{\partial t} \leq 0$, the system is globally stable [54], [55] (in our formulation, the number of intervals are equal to the effect of time in [52],

i.e. $t = k$). For the system E_c is always positive, thus we only need to study the effect of X^o on $\frac{\partial E_c}{\partial k}$

$$
\frac{\partial E_c}{\partial k}(X^o) = \frac{\partial E_c}{\partial X}(X^o)\frac{\partial X}{\partial k}(X^o)
$$
$$
= 2\left(\underline{A}_k X_k^{o2} - B_{c_k}\right)\left(2\underline{A}_k X_k^o\right)^T \frac{X_k^o - X_{k-1}^o}{\Delta k} \leq 0
$$
$$(26)$$

where $\Delta k = 1$, $X_k^o = \frac{\underline{A}_k^T B_{c_k}}{\underline{A}_k^T \underline{A}_k}$, and $X_{k-1}^o = \frac{\underline{A}_{k-1}^T B_{c_{k-1}}}{\underline{A}_{k-1}^T \underline{A}_{k-1}}$ then

$$
\frac{\partial E_c}{\partial k}(X^o) = 2\left(\underline{A}_k\left(\frac{\underline{A}_k^T B_{c_k}}{\underline{A}_k^T \underline{A}_k}\right)^2 - B_{c_k}\right)
$$
$$
\times\left(2\underline{A}_k\frac{\underline{A}_k^T B_{c_k}}{\underline{A}_k^T \underline{A}_k}\right)^T\left(\frac{\underline{A}_k^T B_{c_k}}{\underline{A}_k^T \underline{A}_k} - \frac{\underline{A}_{k-1}^T B_{c_{k-1}}}{\underline{A}_{k-1}^T \underline{A}_{k-1}}\right) \leq 0
$$
$$
= 4\left(\frac{B_{c_k}^2}{\underline{A}_k} - B_{c_k}\right)B_{c_k}^T\left(\frac{B_{c_k}}{\underline{A}_k} - \frac{B_{c_{k-1}}}{\underline{A}_{k-1}}\right) \leq 0
$$
$$
= 4\left(\frac{B_{c_k}}{\underline{A}_k} - I\right)\left(B_{c_k}B_{c_k}^T\right)\left(\frac{B_{c_k}}{\underline{A}_k} - \frac{B_{c_{k-1}}}{\underline{A}_{k-1}}\right) \leq 0
$$
$$(27)$$

Here $\left(B_{c_k}B_{c_k}^T\right)$ is always positive, thus if $\left(\frac{B_{c_k}}{\underline{A}_k} - I\right)\left(\frac{B_{c_k}}{\underline{A}_k} - \frac{B_{c_{k-1}}}{\underline{A}_{k-1}}\right) \leq 0$, the system is stable. In this case, we have two scenarios for $\left(\frac{B_{c_k}}{\underline{A}_k}\right)$ and $\left(\frac{B_{c_{k-1}}}{\underline{A}_{k-1}}\right)$:
Scenario 1:

$$
\frac{B_{c_{k-1}}}{\underline{A}_{k-1}} \leq \frac{B_{c_k}}{\underline{A}_k} \leq I \tag{28}
$$

and **Scenario 2**:

$$
I \leq \frac{B_{c_k}}{\underline{A}_k} \leq \frac{B_{c_{k-1}}}{\underline{A}_{k-1}} \tag{29}
$$

Discussion: For an arbitrary point P, from (14), relative $\underline{A}$ $\underline{C}$ can be considered as following, while $\frac{B_c}{\underline{A}} = \frac{(B + K_{target})}{\underline{A}\ \underline{C}}$:

$$
(\underline{A}\ \underline{C})_p = \frac{3\pi}{2}\frac{\sum\frac{(D_{P_i} - D_p)(D_{P_{i+1}} - D_p)}{\|\vec{P}_i - \vec{P}\|\|\vec{P}_{i+1} - \vec{P}\|}}{\sum\mathcal{A}(f_i)} \tag{30}
$$

Suppose

$$
r_p = \frac{\left\|\vec{P}_i^0 - \vec{P}^0\right\|\left\|\vec{P}_{i+1}^0 - \vec{P}^0\right\|}{\left\|\vec{P}_i - \vec{P}\right\|\left\|\vec{P}_{i+1} - \vec{P}\right\|} \tag{31}
$$

where $\vec{P}^0$, $\vec{P}_i^0$, and $\vec{P}_{i+1}^0$ belong to $\mathcal{S}$ before registration, Eq. (30) can be denoted as:

$$
(\underline{A}\ \underline{C})_P = \frac{3\pi}{2}\frac{\sum\frac{(D_{P_i} - D_p)(D_{P_{i+1}} - D_p)}{\|\vec{P}_i^0 - \vec{P}^0\|\|\vec{P}_{i+1}^0 - \vec{P}^0\|} r_p}{\sum\mathcal{A}(f_i)}
$$
$$
= \frac{3\pi}{2}\frac{\sum cos(\alpha_i^0)\ r_p}{\sum\mathcal{A}(f_i)} \tag{32}
$$

where α_i^0 belongs to f_i in Fig. 3(a) before registration. Considering $(\underline{B})_P$ as in Eq. (19)

$$
\frac{B_c}{\underline{A}} = \frac{\frac{-6\pi + \frac{3\pi}{2}\sum 1}{\sum\mathcal{A}(f_i)} + K_{target_P}}{\frac{3\pi}{2}\frac{\sum cos(\alpha_i^0)\ r_p}{\sum\mathcal{A}(f_i)}} \tag{33}
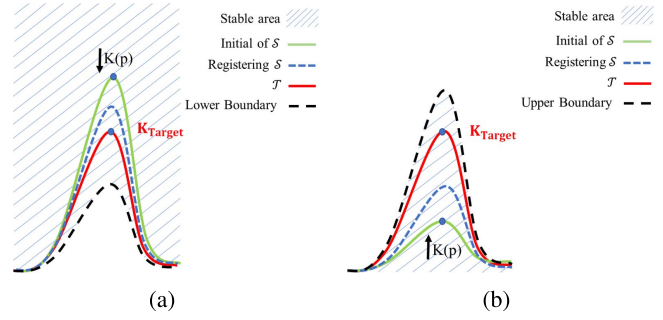$$

Fig. 5. Stability boundaries. (a) Lower boundary for Scenario 1. (b) Upper boundary for Scenario 2.

where K_{target_P} is the semi-curvature value of the corresponding point for P on $\mathcal{T}$. Thus,

$$
\Delta\left(\frac{B_c}{\underline{A}}\right) \propto -\Delta K \tag{34}
$$

2) Scenario 1: The proposed condition in Eq. (28) happens only when $\frac{B_{c_{k-1}}}{\underline{A}_{k-1}} \leq \frac{B_{c_k}}{\underline{A}_k}$, which means $K_{k-1}(P) \geq K_k(P)$ from Eq. (34). And, curvature in point P is decreasing, according to Fig. 5(a). Replacing Eq. (33) by Eq. (28), we will have

$$
\frac{-6\pi + \frac{3\pi}{2}\sum 1}{\sum\mathcal{A}(f_i)} + K_{target_P} \leq \frac{3\pi}{2}\frac{\sum cos(\alpha_i^0)\ r_p}{\sum\mathcal{A}(f_i)} \tag{35}
$$

Adding $-\frac{3\pi}{2}\frac{\sum cos(\alpha_i)}{\sum\mathcal{A}(f_i)}$ to both sides of the above equation, and from Eq. (4)

$$
K(P) - K_{target_p} \geq \frac{3\pi}{2}\frac{\sum cos(\alpha_i) - cos(\alpha_i^0)\ r_p}{\sum\mathcal{A}(f_i)} \tag{36}
$$

This formula indicates that if the semi-curvature in point P is decreasing to reach the value of the semi-curvature of the corresponding point on $\mathcal{T}$, there is a lower limit for stability condition which is less than K_{target_P}.

3) Scenario 2: Using the same procedure as Scenario 1 and replacing Eq. (33) by Eq. (29), we will have

$$
K(P) - K_{target_p} \leq \frac{3\pi}{2}\frac{\sum cos(\alpha_i) - cos(\alpha_i^0)\ r_p}{\sum\mathcal{A}(f_i)} \tag{37}
$$

This formula means that if the semi-curvature in point P increases to reach the value of the semi-curvature of the corresponding point on $\mathcal{T}$, as shown in Fig. 5(b), there is an upper limitation for stability condition, which is greater than K_{target_p}. The stability discussion in both scenarios explains an asymptotically stable approach for the optimal problem. According to [52], any system which is asymptotically stable is also convergent while the states are in their region of attractions which holds for the system discussed here.

To guarantee the stability, for the points that satisfy the criteria, we consider $W_c(P) = 1$, as the semi-curvature term is stable, otherwise $W_c(P) = 0$. Thus, the complete quadratic cost function can be considered as

$$
E(X) = \left\|\begin{bmatrix}\lambda M \otimes G \\ WD \\ \beta W_c A_c\end{bmatrix}X - \begin{bmatrix}0 \\ WU \\ \beta W_c B_c\end{bmatrix}\right\|_F^2
$$
$$
= \|AX - B\|_F^2 \tag{38}
$$

Algorithm 1 The Proposed Non-Rigid ICP Approach

Input: $X \in \mathcal{R}^{4n \times 3}$, $K \in \mathcal{R}^{n \times 1}$, and $K_{target} \in \mathcal{R}^{m \times 1}$
Output: $X_{optimal}$ to minimize $E(X)$ in Eq. (38)

1: **Initialization**
2: $k = 1$
3: **while** $k \leq k^{\max}$ **do**
4:     $j = 1$
5:     **while** $\|X^{k,j} - X^{k,j-1}\| < \epsilon$ or $j < j^{\max}$ **do**
6:         $N(k)$ number of closest u on $\mathcal{T}$ to v_j on $\mathcal{S}(X^{k,j})$ ($[N(k) \in N_r n : N_{mean}]$)
7:         $N_{normal}(k)$ number of closest angle (among previous step), between normal vector of u with v_j ($N_{normal}(k) \in [min(M_{normal}, N(1)) : N_{mean}]$)
8:         N_{mean} number of u (among previous step), with lower H in Eq. (5)
9:         $u_{corresponded}(j)$ = average of previous step
10:         $X^{k,j} = \frac{A^T B}{A^T A}$; ($A, B$ in (38))
11:         $j = j + 1$
12:     **end while**
13:     $X^k_{optimal} = X^{k,j}$
14:     $k = k + 1$
15: **end while**

Note that to integrate B_c in Eq. (38), we change the dimension of $\underline{C}^{-1}$ in Eq. (24) from $n \times 4n$ to $n \times 3$. Where $B_c = (\underline{B} + \overline{K_{target}})\underline{C}^{-1}$, as the components are like matrix D, and accordingly $\underline{C}^{-1}$ is a sparse matrix.

Summarizing the process of establishing the correspondence and minimizing the cost function, that are both defined on the newly introduced semi-curvature, we propose Algorithm 1 to detail the process presented in Fig. 2 for describing the proposed non-rigid ICP approach. In the algorithm, for each iteration with constant number of corresponding points and optimization parameters, the optimization process continues in an inner loop, until the changes in new X is less than a threshold of ϵ or the number of iterations in the inner loop exceeds a defined number as $j^{\max}$.

IV. EXPERIMENT SETUP

A. Data-Set

In the experiment, besides simple geometrical shapes, the human foot, the lumbar vertebrae and the full human body are selected as typical geometric shapes for evaluating the proposed method. Data of those geometric shapes are collected from several data-sets. The first data-set being used is the SHREC'14 data-set [56], in which we selected the feet in data-set number 25 as the source surface. Before the experiment, the meshes of both feet were pre-processed to have a more uniform mesh using ACVD, a freely available software provided by Valette *et al.* [57]. Finally, two meshes, each with 5000 vertices, were used as the inputs of the experiment.

The second data-set is part of the 3D DINED data-sets [58], consisting of 22 high-resolution 3D scans of foot (left and right) obtained from 11 people (4 females and 7 males). 3D scans were acquired by two Artec EVA scanners [59]. Before registration, we re-meshed the scans with the same method used for SHREC'14 and the number of vertices for each mesh is set as 10000.

To evaluate the proposed approach on more complicated freeform surfaces, two lumbar vertebrae were extracted from the data-set presented in [60], which includes a total of 86 models of lumbar vertebrae. In the data-set, lumbar vertebrae are mainly labelled by the prefix L and numbered 1 to 5 (e.g,. $L_4 - 20$ belongs to lumbar number 4 and case 20). We selected $L_4 - 20$ as the source surface and $L_1 - 17$, $L_1 - 18$, $L_1 - 19$ and $L_1 - 21$ as the target surfaces. The source is re-meshed to 20000 vertices through [57], and the targets are re-meshed to 8000 using the same method.

The full human body scans are selected from the Civilian American and European Surface Anthropometry Resource (CAESAR) data-set [61] as they are natural scans with holes, missed parts and natural noise which makes it suitable for assessment. In detail, the CAESAR data-set contains 3D human full body scans of the civilian populations of three North Atlantic Treaty Organization (NATO) countries; the United States of America (USA), The Netherlands, and Italy [61]. In this study, we selected the first 101 scans from the Dutch population as the target surface and evaluated through the predefined landmarks in each mesh. 74 landmarks are explained in [61] (from page 17 to page 30), while we used 73 of them (LM74 as butt block is neglected). For the source mesh, we used the full body template included in the Wrap 3 software [62].

B. Parameters of the Proposed Method

Table I presents parameters used in the experiment. In establishing the correspondence, the algorithm is designed to emphasise on the semi-curvature at the beginning, and ends on the closest Euclidean distances to find the correspondence point. Thus, ζ changed from 0 to 1, and $1 - \zeta^\eta$ changed from 1 to 0, regarding to Table I.

During the minimization of the cost function, γ in G introduced in Section III-D.1, was chosen to one. λ, named as gradual relaxation of the stiffness constraint, was employed for each method, decreasing from 1000 to 1. Regarding dependency of λ values to the dynamic of source surface, this value was manually defined so that only global deformations were considered in the beginning of registration. On the other hand, the lower limit of λ also depends on the data type [39]. Accordingly, a small λ may cause singularity of A in Eq. (38), which leads to instability of the solution. Therefore, our experiments started with a sufficiently high λ. A high value of λ was not problematic as λ had no effect on quality of the registration results, however more steps were expected, e.g. in Table I, λ varied from 1000 to 1 in 20 iterations. As we want to have a fine match for the points with a larger weight on semi-curvature in the beginning but more emphasis on the distance at the end, we set the values of β using the similar strategy as in specifying λ, i.e. gradually reducing it from 1000 to 1 as shown in Table I.

TABLE I
PARAMETERS USED IN SIMULATION CONFIGURATION

Parameter	Value	Description
$\lambda(k)$	1000:1	Stiffness trade-off
$\beta(k)$	1000:1	Semi-curvature trade-off
$\zeta(k)$	0:1	Distance gain in Eq.(5)
η	1	ζ power in Eq.(5)
N_{mean}	3	Target points averaging size
N_r	0.1	Initial ratio of n points on $\mathcal{S}$
$N(k)$	$N_r n : N_{mean}$	Target points pool size
M_{normal}	20	Initial number of the middle region members
$N_{normal}(k)$	$M_{normal} : N_{mean}$	Pool size for points with similar normal
ϵ	0.001	Convergence error threshold
$j^{\max}$	50	Convergence iteration threshold
$k^{\max}$	20	Number of iteration for the outer loop in Algorithm 1

To have a smoother registration process, we were averaging a number of points from a set with size of 3 ($N_{mean} = 3$). This N_{mean} number of points were offered by H in Eq. (5). Emphasizing on the semi-curvature at the beginning and the closest Euclidean distance at the end of simulation, N number of points on $\mathcal{T}$ in Algorithm 1, as a region to search for corresponding point to any vertices on $\mathcal{S}$, changed from 10 % of the total number of vertices in $\mathcal{T}$ to N_{mean}.

In the implementation of [63], the system of linear equations that arises in each step was solved with the help of the UMFPACK library [64].

C. Other Methods for Comparison

In the experiment, we compared the performance of the proposed method with existing methods proposed by Amberg *et al.* [39], Lee *et al.* [65], Vestner *et al.* [66], Andriy *et al.* [67] and Hirose [26]. Briefly, Amberg's method accounts for an optimal step non-rigid ICP approach capable to employ different regularisations, while they are using a range of lowering stiffness parameter. However, the semi-curvature is not used. As the proposed method is based on Amberg's method, therefore in the implementation of Amberg's method, we removed the semi-curvature information from our method, i.e. the cost function of Eq. (10) and Eq. (12) are changed to:

$$E(X) = \left\| \begin{bmatrix} \gamma \, M \otimes G \\ W D \end{bmatrix} X - \begin{bmatrix} 0 \\ W U \end{bmatrix} \right\|_F^2 \qquad (39)$$

Then Eq. (38) is employed for utilizing the semi-curvature in the non-rigid ICP registration.

Lee's method is able to establish correspondences between non-rigidly deformed shapes through mapping the shape to a unit Möbius sphere by centered conformal parameterization. Ultimately, they exert Fast Fourier Transformation (FFT) to detect the optimal rotational alignment between sphere meshes and perfect the registration process through optical flow. However, their method only works for Genus-zero shapes,

which is a limitation. The executable source code used in this paper, is available in [68].

Vestner' method presents a methodology to specify the correspondences between two shapes which may be non-isometric shapes. The method uses kernel instead of distance as the descriptor, which makes the approach more sensitive to the quality of the mesh and the triangles size. The executable source code used in this paper, is available in [69].

Andriy introduced the CPD algorithm [67] employing Gaussian radial basis functions as a replacement for thin-plate splines which addresses a different version of regularizer. In the method, the rigid and non-rigid registrations are covered, while the approach is ill suited to account for a considerably large amount of outliers and in exploring among all the possible correspondences which is in general Non-deterministic Polynomial-time hard (NP-hard). The executable source code used in this paper, is available in [70].

Hirose proposed the BCPD method [26], using variational Bayesian inference theory to explain the coherent drift. The executable source code used in this paper, is available in [71]. All algorithms were implemented using Matlab®R2020a on a computing platform with an Intel® Core-i5™ 9600K 4.6 GHz processor.

V. EXPERIMENT RESULTS

A. Effect of Curvature Term During Registration

In this subsection, through a few experiments using some basic shapes, we investigate the effect of the semi-curvature term on the feature preservation after registration in terms of correspondences, and the mesh quality, especially for highly curved area.

1) Feature Preservation: As we want to observe the effects of with and without the semi-curvature term, only Amberg's method and the proposed method were used. When the stiffness term is sufficiently low, in each iteration, the surface can be changed, and consequently the original curvature of the source surface will be changed. This causes an error in establishing the correspondences through Eq. (5). In this case the semi-curvature term contributes an additional logical connection between vertices and their neighbors, over the stiffness term to increased smoothness. Apparently, the improvements in high-curved areas are more visible than the flat areas due to the properties of the semi-curvature. To show the effect, a shape with ellipsoidal cross-section (gray) is used as $\mathcal{S}$, a shape with spherical cross-section (green) is employed as $\mathcal{T}$, and a colourful mesh of $\mathcal{S}$ is utilized shown in Fig. 6. Fig. 6(a) shows the initial condition, Fig. 6(b) presents the registration through Eq. (38) and H in Eq. (5), and Fig. 6(c) presents the registration through Eq. (38) without semi-curvature term and the H. A comparison of Fig. 6(b) and (c) reveals that the ellipsoidal shape is preserved for all cross-sections when E_c is used due to both the additional meaningful connections of the neighbouring vertices and more the meaningful correspondences selection. The results are also more visible in the colorful graphs of Fig. 6 left column, that the colors on the spherical cross-section without the semi-curvature are
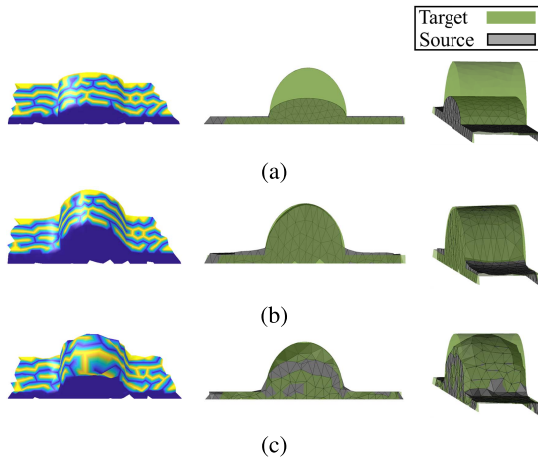
Fig. 6.   Curved shape preservation experiment (a) The initial setup (b) Registration using the proposed method (with the semi-curvature term). (c) Registration using Amberg's method (without the semi-curvature term).

stretched and less preserved than the results with the semi-curvature.

2) Missing Parts and Sparse / Dense Mesh: Using the proposed method, although we find more constraints for neighboring vertices of each point on source, extra unnecessary connections are also deleted based on H. After finding the correspondences, the number of connections to the corresponding points on the target is checked and if they are more than N_{mean}, we choose N_{mean} of them with minimum H. This correction avoids registering the points on source which are describing the missed part on the target. Only, they are wisely deformed based on stiffness term, and the semi-curvature term guarantees the uniform shape on the borders of the missed part. This is shown in Fig. 7. In this experiment, Fig. 7(a) shows the initial condition, Fig. 7(b) defines the effects of curvature term on quality of registration for the missed part, and 7(c) depicts the registration without the semi-curvature term. Moreover, wisely deleting connections based on H preserves the original mesh detail (shape of the faces) and uniformity of the surfaces which is addressed by the semi-curvature term. Thus, the final registered mesh is very different from the target and the resolution is equal to the original source surface. The results can be explored through the shaded graphs showing that the semi-curvature term preserved the mesh structure for the missed part (Fig. 7(b)(left)) as the faces with blue color is stretched around the missing part when the semi-curvature is not used (Fig. 7(c)(left)). A comparison of Fig. 7(d)(left) with Fig. 7(d)(right) reveals that without the semi-curvature term in both H and E, the final mesh is going to be degenerate (i.e. the collapse into zero area faces) and some points have the same geometry. The degeneration happens when number of source vertices is higher than number of target vertices, thus many points on the source have the same corresponding points.

B. Validation: The Foot Scans

1) Registration Process and Results: Fig. 8 depicts the source ($\mathcal{S}$) and the target surfaces ($\mathcal{T}$) used in the registration.
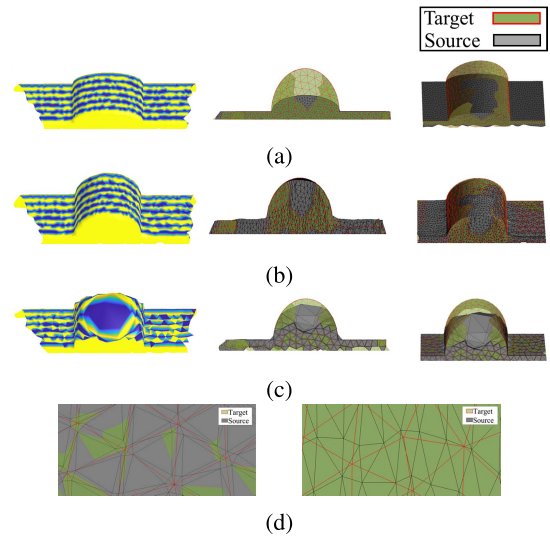

Fig. 7.   Missed part experiment (a) The initial setup (b) The proposed method (with the semi-curvature term). (c) Amberg's method (without the semi-curvature term) (d) Mesh quality: Amberg's method (left), The proposed method (with the semi-curvature term) (right).
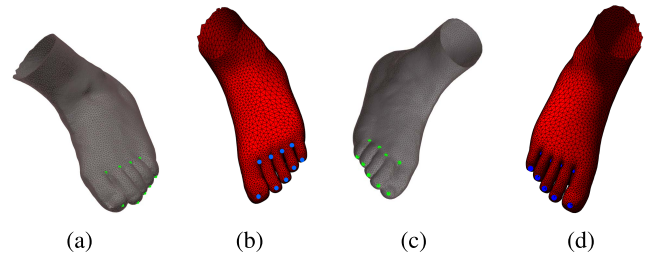

Fig. 8.   Meshes and LMs. (a) Target surface ($\mathcal{T}$) of left foot. (b) Source surface ($\mathcal{S}$) of left foot. (c) Target surface ($\mathcal{T}$) of right foot. (d) Source surface ($\mathcal{S}$) of right foot.
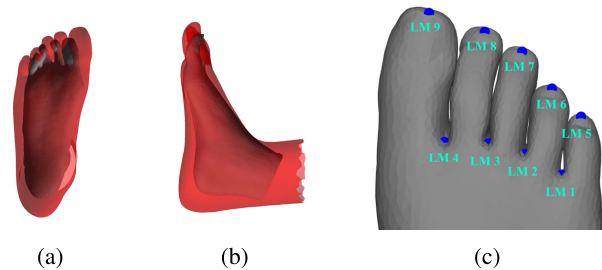

Fig. 9.   The initial setup: (a) Front view, (b) Side view. (c) LMs location on a sample foot.

In the figure, location of manually defined LMs on the right/left foot are highlighted and those LMs are used to evaluate the registration results of using different methods. In all experiments, the initial conditions (Fig. 9) are kept the same for a more accurate comparison.

The difference between landmarks in the registered $\mathcal{S}$ and the corresponding landmarks in the $\mathcal{T}$ represents the accuracy of the registration, which can be highly benefited from a non-rigid ICP method incorporated with a meaningful correspondence selection method and a robust convergence.
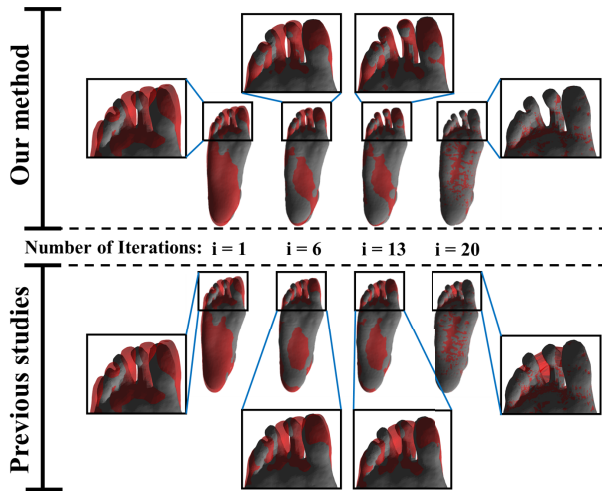
Fig. 10. Registration results. Proposed method (top), Amberg's method (bottom).

Fig. 11. LM location comparison. (a) Amberg's method. (b) Lee's method. (c) Vestner's method. (d) CPD method. (e). BCPD method. (f) Our method.

Fig. 12. (a) Percentage correspondences according to registration error. (b) RMSE distribution.

For this, we defined a series of LM_j on all meshes as depicted in Fig. 9(c), where $j = 1, \ldots, 9$. The registration results in different steps ($i = 1, 6, 13,$ and 20) of using the algorithms with/without semi-curvature (Amberg/our method) are presented in Fig. 10. In the figure, it can be found that the proposed method is more robust against the interference of geometries in the toe area, which is clearly visible after $i = 13$. In Fig. 11, the registered $\mathcal{T}$ and $\mathcal{S}$ using Amberg's method, Lee's method, Vestner' method, the CPD method, the BCPD method and our approach are presented with the LMs, respectively. In the figure, green points represents LMs on $\mathcal{T}$ and black ones are LMS on $\mathcal{S}$ (only for Vestner' method, both the green and black points are on the target, as the approach only defines the correspondences and does not support any registration). It can be found that at the final stage there is a considerable distance between final black and green points in Fig. 11(a)(b)(d)(e), especially for the tip of mid-toe compared to Fig. 11(f), which utilizes our method.

Geometry-wise, there are many metrics used in evaluating the performance of the non-rigid ICP algorithm, such as Mean Absolute Error (MAE) [72], Root Mean Square Error (RMSE) [73], mean S value [12], average F1-measure (F1) [12] according to different applications. Among those, we investigate the RMSE metric for all the points on the registered $\mathcal{S}$, MAE for the landmarks and mesh quality values which allow us to evaluate the level of geometry preservation and accuracy. The foot registration results and the error of the LMs are reported in Table II(a), where average Diagonal of the Bounding Box (DBB) for $\mathcal{S}$ for the source mesh is 362.63 mm. These results imply that not only the mean error of the proposed method is less, the standard deviations (SD) of errors are smaller as well. Accordingly, the semi-curvature term could offer more accurate corresponding points which means that the final transformed source points (black) are more close to the optimal positions (green). The major reason is that the proposed algorithm is more sensitive for points with higher curvature and usually flat areas (low curved points) are least likely to have LMs. Finally, the overall error per method in
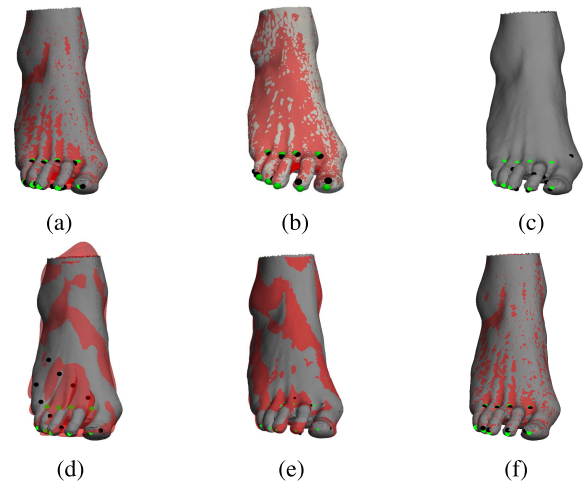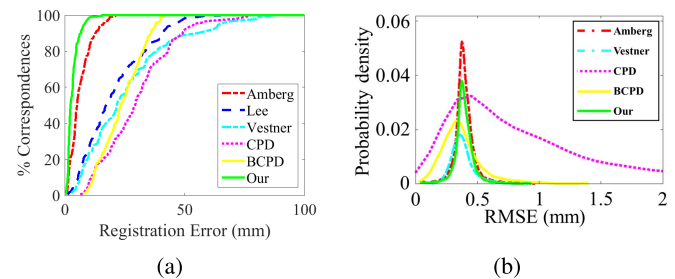
the table leads us to the conclusion that the proposed method is more accurate with less error and less SD.

Figure 12(a) depicts the percentage of correspondences including all 9 selected landmarks for all the 22 scans (y-axis) that have less distance error than a threshold (x-axis) [74]. Regarding the figure, our method (green line) detects the correspondences earlier than the other five methods, and the errors are lower than 10 mm, while for Amberg (red line), Lee (blue line), Vestner (cyan line), CPD (purple line), and BCPD (yellow line), they are 25 mm, 68 mm, 88 mm, 75 mm, and 43 mm, respectively. The results confirm that the proposed methodology has better accuracy and robustness compared to other methods. Figure 12(b) shows the probability density based on the RMSE of each point on the registered $\mathcal{S}$ and the closest point on the $\mathcal{T}$ along the 22 scans. As can be seen Amberg (red) has the least spread and CPD has the largest sparsity in terms of closest point, this is because Amberg has no term to keep the original geometry of $\mathcal{S}$. Besides the error, our method has the least error of correspondences and acceptable level of the source mesh geometry preservation.

2) Mesh Quality: Deformations of the computational mesh arising from optimization routines usually lead to a decrease of mesh quality or even destruction of the mesh [75]. Mesh quality is representative for various quality metrics for the shape of mesh elements [76], such as dihedral angles [77], the longest edge over the in-radius [78], and shape of the elements

TABLE II

FOOT REGISTRATION RESULTS

a) Overall LM mean error $\pm$ Standard Deviation (SD) (mm) result.					
Mean DBB of $\mathcal{S}$ = 362.63 mm					
	Amberg [39]	Lee [65]	Vestner [66]	CPD [67]	BCPD [26]	Our method
LM 1	5.9±4.4	20.3±14.5	29.4±23.3	41.4±18.1	24.1±19.3	**3.5±2.3**
LM 2	6.1±4.7	23.3±15.8	21.3±10.5	33.2±21.4	25.8±10.8	**2.9±3.1**
LM 3	5.1±4.1	26.4±18.2	20.3±10.6	28.5±22.5	25.6±11.9	**2.3±1.5**
LM 4	5.4±3.4	25.9±16.1	23.8±22.4	16.3±12.6	23.3±20.1	**3.0±1.9**
LM 5	6.7±5.2	18.9±12.1	39.1±31.9	54.7±27.9	14.1±9.9	**3.0±2.2**
LM 6	6.5±4.6	21.6±9.4	27.9±13.9	35.3±14.3	23.2±12.4	**3.3±2.1**
LM 7	7.6±5.3	21.5±8.1	25.9±9.7	22.8±16.6	21.1±8.5	**3.1±1.8**
LM 8	8.3±5.3	19.9±10.1	28.1±16.2	10.9±8.3	24.2±16.1	**3.7±3.6**
LM 9	6.0±2.9	7.3±4.1	21.3±22.8	8.9±6.2	12.9±7.7	**4.8±2.6**
Overall	6.4±4.5	20.6±13.6	26.3±19.2	30.5±15.3	21.6±8.9	**3.3±2.5**
b) Mesh quality mean value $\pm$ Standard Deviation (SD).					
Original mesh	Amberg [39]	Lee [65]	Vestner [66]	CPD [67]	BCPD [26]	Our method
0.92±0.07	0.51±0.48	0.65±0.33	NaN	0.71±0.25	0.78±0.16	**0.83±0.13**
c) The complete process computing time (s).					
	Amberg [39]	Lee [65]	Vestner [66]	CPD [67]	BCPD [26]	Our method
Time (s)	**9.3**	32.7	28.4	1266.5	680.3	17.1

and smoothness [79]. Among various methods, we employ Liu and Joe's parameter approach [80] to compare the quality of meshes. The approach defines the quality per vertex (average of the mesh quality of the faces incident to the vertex) with a number between 0 and 1, in which 1 is the best quality and zero is the least quality. The mesh quality of a mesh is calculated as the mean of the quality of all vertices in the mesh. Accordingly, the mesh quality of registration results is reported in TABLE II(b), where the mean and SD of the mesh quality of 22 original scans, and the mesh quality of the registration results using six methods are presented, respectively. The table defines 44%, 29%, 23% 15%, and 10% mesh quality loss for Amberg's method, Lee's method, the CPD method, the BCPD method and our approach respectively. As the output of Vestner' method is only the set of corresponded vertex ids, the mesh quality is not applicable.

3) Run Time Discussion: The computing speed is used as the criterion to evaluate the efficiency of each mentioned method. Accordingly, here we report the average of computing time of the whole process for all the experiments in Table II(c). The proposed method is slower than Amberg's methods for the complete process, which is mainly caused by the extra computing needed for the introduced semi-curvature term in Eq. (39). However, the needed computing times for minimizing the cost function are similar, 6.48 (s) for Amberg's method and 6.19 (s) for our method. It can be inferred that using the proposed method reduces 48% of the error at the cost of nearly same computing time for minimization. As Lee's method, Vestner' method, CPD, and BCPD take more computing time and the results are less accurate, it indicates that the proposed method is acceptable regarding the computing time, mainly due to the improved accuracy.

4) Sensitivity Analysis: We initially perform a set of experiments using the 3D DINED data-sets of foot in [58] to investigate the sensitivity of the parameters λ, β, N_r and N_{normal}, and η for selecting the proper range of parameters [81]. As can be seen from Fig. 13, which shows how

the obtained LM error varies by altering, in pairs, the weights used in the cost function Eq. (38), the method is capable of obtaining a low the error value (blue areas) for a wide range of those parameters. This indicates the robustness level of the method, as it is less sensitive to the choice of the range of parameters. Theoretically, the robustness is expected as discussed in Section III-E, the system is stable for the region of Eq. (36) and (37), which are infinite from one side. The robustness is desirable for practical applications, since it implies there is no need for fine tuning in order to achieve satisfactory results.

To investigate the effect of η, we show the average error of LMs for the all foot scans in Fig. 13(e) based on MAE error of LMs and the SD. The error is minimal when η is equal to 1. If the value of η is in other regions, the errors might increase, however, it is still stable.

C. Validation: The Lumbar Vertebra & the Full Body

In line with Subsection V-B, to evaluate the performance of the proposed method, we implement the method on the lumbar vertebrae data set and the full body explained in section IV-A.

1) The Lumbar Vertebra: Using the same method in the previous section, we register the lumbar vertebra of $L_4 - 20$ in section IV-A on the lumbar vertebrae of $L_1 - 17$, $L_1 - 18$, $L_1 - 19$ and $L_1 - 21$ using Amberg's method, the CPD method, the BCPD method and the proposed method. Lee's method is excluded since it is limited to genus 0 topology.

In all three experiments, the initial conditions for the four methods are the same. As an example, the initial condition of the $L_4 - 20$, and the $L_1 - 17$ is presented in Fig. 14. For the assessment, we used 16 landmarks as shown in Fig. 15. The registration results of using the four methods are compared in Fig. 16, where in the target column of Fig. 16, the quality of correspondences of LMs can be visualized with four highlighted areas. In the initial conditions, the foramen on the source surface is much smaller than the target and located on top of the target's foramen, and as Amberg's
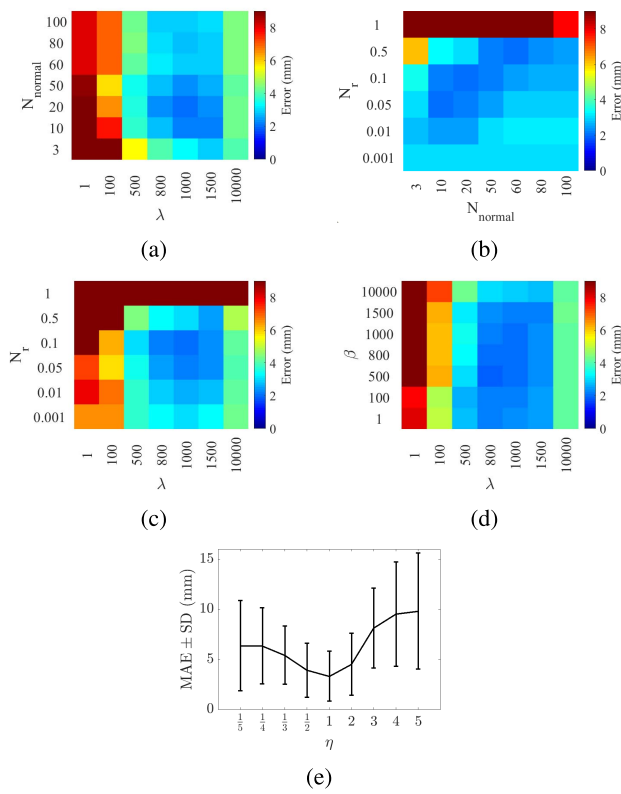
Fig. 13. Sensitivity analysis showing error of the LMs for: (a) a domain of λ and N_{normal}, while $N_r = 0.1$; (b) a domain of N_{normal} and N_r, while $\lambda = 1000$; (c) a domain of λ and N_r, while $N_{normal} = 20$; (d) a domain of λ and β, while $N_{normal} = 20$, $N_r = 0.1$. (e) Sensitivity of error the LMs on η.
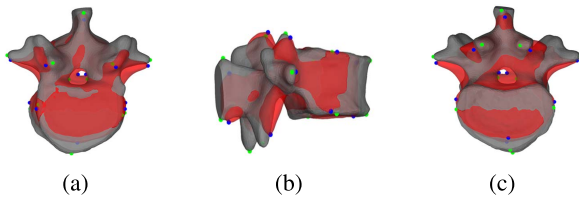

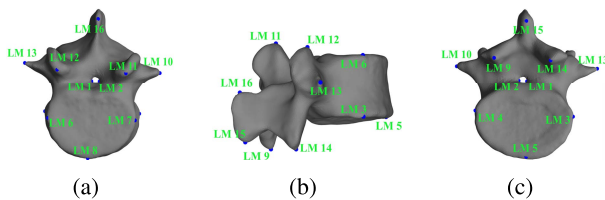Fig. 14. Lumbar initial condition.

Fig. 15. LM location in lumbar. (a) Top view. (b) 3D view (c) Bottom view.

method uses closest distance to find the correspondences, the points may get stuck there and the hole disappears. However, the semi-curvature term can distinguish the differences as the curvature values are different. For the other two selected areas on the left-middle vertebra, the proposed method also outperforms Amberg's method in preserving regions with high curvature.
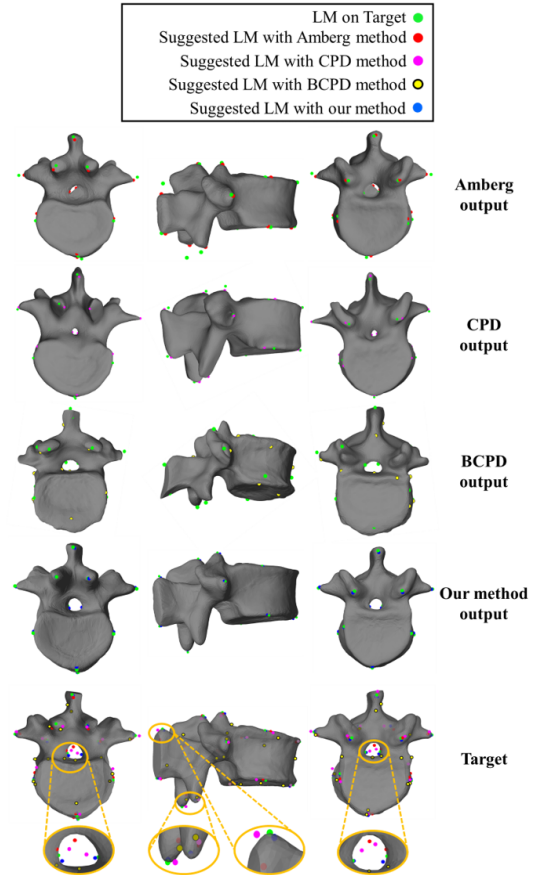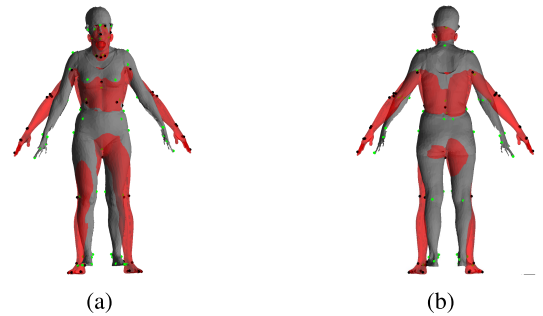

Fig. 16. Lumbar registration.

Fig. 17. Full body initial condition. (a) Front view. (b) Back view.

Errors between corresponding landmarks are reported in TABLE III(a) where our method outperforms Amberg's method, CPD method, and BCPD method by 58%, 87%, and 81% respectively regarding the mean absolute error. Moreover, our approach, the CPD method, and the BCPD method preserved the same mesh quality with only 2% quality loss comparing to the original mesh reported in TABLE III(b). However, Amberg's method lost 23% of the original mesh quality during the registration. TABLE III(c) indicates that using the CPD method is very time consuming as the time duration for the experiment is about 8700%, 13400%, and 212% more than our method, Amberg's method, and the BCPD method.

2) The Full Body: Similar to the lumbar vertebra registration, we repeated the experiments with full human body

TABLE III
LUMBAR VERTEBRA REGISTRATION RESULTS

a) Overall LM mean error ±Standard Deviation (SD) (mm) result.

Landmark ID	Amberg [39]	CPD [67]	BCPD [26]	Our method
	DBB of $\mathcal{S}$ = 90 mm			
LM 1	6.9±4.4	8.5±2.1	10.5±3.7	**3.2±0.5**
LM 2	3.8±2.7	8.3±3.9	10.2±4.4	**0.8±0.4**
LM 3	2.5±0.7	7.9±4.1	5.7±3.8	**1.2±0.4**
LM 4	2.3±1.4	10.3±1.1	5.9±2.1	**1.1±0.5**
LM 5	**2.0±1.5**	9.5±2.5	8.8±3.1	2.3±0.9
LM 6	3.2±1.3	8.2±2.3	7.3±1.9	**1.1±0.9**
LM 7	2.5±0.5	10.9±3.3	12.8±2.7	**1.1±0.9**
LM 8	1.9±1.2	8.8±3.6	5.1±1.5	**1.1±1.6**
LM 9	5.4±2.3	9.2±3.9	7.4±2.5	**0.9±0.4**
LM 10	3.9±1.6	11.1±1.5	5.9±2.2	**2.8±2.6**
LM 11	3.3±3.1	11.8±3.5	6.6±1.8	**1.4±0.3**
LM 12	3.9±3.5	8.8±3.4	8.2±4.8	**1.7±0.7**
LM 13	2.2±1.9	7.9±0.9	8.2±1.1	**0.8±0.2**
LM 14	4.1±2.9	7.9±0.7	6.5±1.1	**1.4±1.5**
LM 15	2.4±0.9	8.6±2.6	5.1±1.3	**0.9±1.1**
LM 16	4.8±2.4	10.2±4.9	9.3±3.6	**1.5±0.6**
Overall (mm)	3.4±2.5	9.2±4.3	7.7±2.9	**1.4±1.2**

b) Mesh quality mean value ±Standard Deviation (SD).

Original mesh	Amberg [39]	CPD [67]	BCPD [26]	Our method
0.8 ±0.14	0.61±0.32	0.77±0.16	**0.78±0.17**	**0.78±0.16**

c) The complete process computing time (s).

	Amberg [39]	CPD [67]	BCPD [26]	Our method
Time (s)	**14.1**	1895	869	21.6

Fig. 18.　Full body registration. (a) Amberg. (b) CPD. (c) BCPD. (d) Our method.

TABLE IV
FULL HUMAN BODY REGISTRATION RESULTS

a) Overall LM mean error ± Standard Deviation (SD) (mm).

Total vertices %	Amberg [39]	CPD [67]	BCPD [26]	Our method
	DBB of $\mathcal{S}$ = 2167.6 mm			
100	31.2±18.9	76.8±98.5	27.7±22.3	**10.6±7.6**
80	31.7±20.0	74.8±100.8	38.4±31.5	**12.4±8.6**
60	31.7±25.9	92.2±104	42.7±28.9	**13.1±12.3**
40	42.5±41.1	135.6±110.8	48.1±34.4	**16.7±12.2**
20	51.9±54.7	190.4±125.6	52.6±50.3	**17.5±20.0**

b) Mesh quality mean value ± Standard Deviation (SD).

Total vertices %	Original mesh	Amberg [39]	CPD [67]	BCPD [26]	Our method
100	0.80±0.15	0.51±0.21	0.67±0.22	**0.69±0.25**	0.68±0.26
80	0.74±0.18	0.49±0.25	**0.74±0.16**	0.71±0.24	0.68±0.25
60	0.72±0.20	0.41±0.29	0.73±0.20	**0.73±0.24**	0.64±0.30
40	0.71±0.21	0.33±0.38	**0.67±0.22**	0.62±0.29	0.61±0.29
20	0.70±0.22	0.31±0.38	0.55±0.25	**0.59±0.31**	0.51±0.42

c) The complete process computing time ± Standard Deviation (SD) (s).

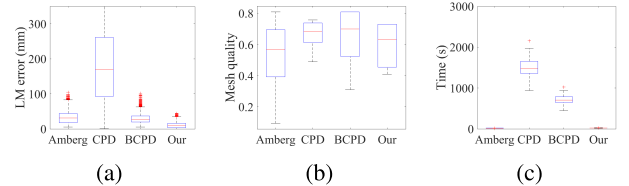| Total vertices %	Amberg [39]	CPD [67]	BCPD [26]	Our method
100	**18.3±1.1**	1567±825	746±393	21.9±2.2
80	**16.7±1.7**	1221±1001	593±408	21.7±1.4
60	**12.5±0.9**	836±758	443±341	19.6±1.3
40	**10.6±1.1**	555±318	342±330	16.5±1.8
20	**7.9±0.4**	489±362	299±271	15.1±0.7

(a)　　　　　　　　(b)　　　　　　　　(c)

Fig. 19.　Boxplots of (a) Landmark error, (b) Mesh quality, and (c) Computing time regarding the full body registration with 100% of the source vertices.

linearly with the number of vertices, while the computing time of using the CPD and BCPD method is increasing exponentially, which often lead to large SD values. Figure 19 presents the boxplots of the registration results of using 100% the vertices of the source surface regarding the three criteria. In Fig. 19(a), the landmark errors of 7373 samples (101 scans × 73 LMs) for each method are shown where our method has the smallest error. Figure 19(b) depicts the mesh quality with 101 samples per method. The results of using our method, the CPD, and the BCPD are in the same range. In terms of the computing time for registering the 101 scans (Fig. 19(c)), registering scans by our and Amberg's methods are in the same range, both are much faster than using the CPD and the BCPD methods.

VI. CONCLUSION

This paper presents a non-rigid ICP approach based on a newly defined semi-curvature. With similar properties to the Gaussian curvature, the semi-curvature has different mathematical and geometric characteristics. Based on these characteristics, we use the semi-curvature as part of the metric in establishing the correspondences and in the cost function, where the distance and the stiffness terms are embedded as well. Moreover, by increasing the logical dependency of vertices on their neighbors, the semi-curvature term preserves the features of a surface in a guaranteed stable region during

with more valid landmarks as validation. The initial condition and the landmarks of both the target and source meshes are depicted in Fig. 17. The registration results are shown in Fig. 18 and discussed in more detail in TABLE IV for different numbers of points in the source mesh. The original source mesh contains 19882 vertices, and the registration results are reported employing the remeshed source mesh with 100%, 80%, 60%, 40%, and 20% of the total vertices of the original source mesh. According to TABLE IV(a), our method presents on average 62%, 86% and 66% less landmark errors comparing to Amberg's method, CPD method, and BCPD method respectively. Moreover, as in TABLE IV(b), the observed mesh quality loss comparing to the original source mesh is on average about 44% for using Amberg's method, 9% for using the CPD and the BCPD methods, and 15% for using our method. Again, TABLE IV(c) indicates that using the CPD method costs more computing time, accounting for 4820%, 6970% and 92% more of using our method, using Amberg's method and using the BCPD method, respectively. Also, the time for our approach and Amberg's approach is increasing

the registration process, emphasising on mesh quality and convergence. Experimental results indicate that the proposed non-rigid ICP approach outperforms existing methods in the area where features are not prominent or there are interferences between/among features, as it is able to use the intrinsic properties of the complete surface during the registration. As the approach introduces a general methodology to integrate any number of linear or nonlinear terms (as long as they are linearisable) in the cost function with guaranteed stable region, we will study the extension of the cost function to other new terms in our future work. Moreover, establishing a logical balance between the deformation and the feature preservation via a time-varying adaptive stiffness term is another future direction. In addition, the semi-curvature is defined based on the 1-ring neighboring points, and the effect of including more rings and robustness to the noise on the target mesh will also be studied in the future research.

REFERENCES

[1] K. Guo, F. Xu, T. Yu, X. Liu, Q. Dai, and Y. Liu, "Real-time geometry, albedo, and motion reconstruction using a single RGB-D camera," *ACM Trans. Graph.*, vol. 36, no. 4, p. 1, Jul. 2017.

[2] I. L. Dryden and K. V. Mardia, *Statistical Shape Analysis: With Applications in R*, vol. 995. Hoboken, NJ, USA: Wiley, 2016.

[3] J. Fan, X. Cao, P.-T. Yap, and D. Shen, "BIRNet: Brain image registration using dual-supervised fully convolutional networks," *Med. Image Anal.*, vol. 54, pp. 193–206, May 2019.

[4] W. G. Aguilar, S. Morales, H. Ruiz, and V. Abad, "RRT* GL based optimal path planning for real-time navigation of UAVs," in *Proc. Int. Workshop-Conf. Artif. Neural Netw.* Cádiz, Spain: Springer, 2017, pp. 585–595.

[5] R. M. Dyke, Y.-K. Lai, P. L. Rosin, and G. K. Tam, "Non-rigid registration under anisotropic deformations," *Comput. Aided Geometric Des.*, vol. 71, pp. 142–156, May 2019.

[6] S. Z. Gilani, K. Rooney, F. Shafait, M. Walters, and A. Mian, "Geometric facial gender scoring: Objectivity of perception," *PLoS ONE*, vol. 9, no. 6, Jun. 2014, Art. no. e99483.

[7] T. Heimann and H.-P. Meinzer, "Statistical shape models for 3D medical image segmentation: A review," *Med. Image Anal.*, vol. 13, no. 4, pp. 543–563, Aug. 2009.

[8] W.-S. Lee and N. Magnenat-Thalmann, "Fast head modeling for animation," *Image Vis. Comput.*, vol. 18, no. 4, pp. 355–364, Mar. 2000.

[9] S. Shirani, "Content-based multiple description image coding," *IEEE Trans. Multimedia*, vol. 8, no. 2, pp. 411–419, Apr. 2006.

[10] S. Marcos, J. Gómez-García-Bermejo, and E. Zalama, "A realistic, virtual head for human–computer interaction," *Interacting Comput.*, vol. 22, no. 3, pp. 176–192, May 2010.

[11] M. Tajdari *et al.*, "Image-based modelling for adolescent idiopathic scoliosis: Mechanistic machine learning analysis and prediction," *Comput. Methods Appl. Mech. Eng.*, vol. 374, Feb. 2021, Art. no. 113590.

[12] S. Cheng, I. Marras, S. Zafeiriou, and M. Pantic, "Statistical non-rigid ICP algorithm and its application to 3D face alignment," *Image Vis. Comput.*, vol. 58, pp. 3–12, Feb. 2017.

[13] D. Kim and D. Kim, "A fast ICP algorithm for 3-D human body motion tracking," *IEEE Signal Process. Lett.*, vol. 17, no. 4, pp. 402–405, Apr. 2010.

[14] I. Toschi, E. M. Farella, M. Welponer, and F. Remondino, "Quality-based registration refinement of airborne LiDAR and photogrammetric point clouds," *ISPRS J. Photogramm. Remote Sens.*, vol. 172, pp. 160–170, Feb. 2021.

[15] R. Gal and D. Cohen-Or, "Salient geometric features for partial shape matching and similarity," *ACM Trans. Graph.*, vol. 25, no. 1, pp. 130–150, Jan. 2006.

[16] M. L. Tazir, T. Gokhool, P. Checchin, L. Malaterre, and L. Trassoudaine, "Cluster ICP: Towards sparse to dense registration," in *Proc. Int. Conf. Intell. Autonomous Syst.* Baden-Baden, Germany: Springer, 2018, pp. 730–747.

[17] K. Li, J. Yang, Y.-K. Lai, and D. Guo, "Robust non-rigid registration with reweighted position and transformation sparsity," *IEEE Trans. Vis. Comput. Graphics*, vol. 25, no. 6, pp. 2255–2269, Jun. 2019.

[18] T. Jiang, K. Qian, S. Liu, J. Wang, X. Yang, and J. Zhang, "Consistent as-similar-as-possible non-isometric surface registration," *Vis. Comput.*, vol. 33, nos. 6–8, pp. 891–901, Jun. 2017.

[19] K. Mori, A. Yukawa, A. Kono, and Y. Hata, "Heart failure diagnosis for tagged magnetic resonance images," in *Proc. Int. Conf. Mach. Learn. Cybern. (ICMLC)*, Jul. 2017, pp. 67–70.

[20] B. Ibragimov and T. Vrtovec, "Landmark-based statistical shape representations," *Stat. Shape Deformation Anal.*, pp. 89–113, Jan. 2017.

[21] Y. Sahillioğlu, "Recent advances in shape correspondence," *Vis. Comput.*, vol. 36, no. 8, pp. 1705–1721, Aug. 2020.

[22] H. Hontani, T. Matsuno, and Y. Sawada, "Robust nonrigid ICP using outlier-sparsity regularization," in *Proc. IEEE Conf. Comput. Vis. Pattern Recognit.*, Jun. 2012, pp. 174–181.

[23] L. Liang *et al.*, "Nonrigid iterative closest points for registration of 3D biomedical surfaces," *Opt. Lasers Eng.*, vol. 100, pp. 141–154, Jan. 2018.

[24] H. Li, R. W. Sumner, and M. Pauly, "Global correspondence optimization for non-rigid registration of depth scans," *Comput. Graph. Forum*, vol. 27, no. 5, pp. 1421–1430, Jul. 2008.

[25] H. Dai, N. Pears, and W. Smith, "Non-rigid 3D shape registration using an adaptive template," in *Proc. Eur. Conf. Comput. Vis. (ECCV)*, 2018, pp. 48–63.

[26] O. Hirose, "A Bayesian formulation of coherent point drift," *IEEE Trans. Pattern Anal. Mach. Intell.*, vol. 43, no. 7, pp. 2269–2286, Jul. 2020.

[27] Z. Yao, Q. Zhao, X. Li, and Q. Bi, "Point cloud registration algorithm based on curvature feature similarity," *Measurement*, vol. 177, Jun. 2021, Art. no. 109274.

[28] K. Guo, F. Xu, Y. Wang, Y. Liu, and Q. Dai, "Robust non-rigid motion tracking and surface reconstruction using l0 regularization," in *Proc. IEEE Int. Conf. Comput. Vis. (ICCV)*, Dec. 2015, pp. 3083–3091.

[29] Y. Yang, T. Yuan, T. Huysmans, W. S. Elkhuizen, F. Tajdari, and Y. Song, "Posture-invariant three dimensional human hand statistical shape model," *J. Comput. Inf. Sci. Eng.*, vol. 21, no. 3, Jun. 2021, Art. no. 031006.

[30] G. C. Sharp, S. W. Lee, and D. K. Wehe, "ICP registration using invariant features," *IEEE Trans. Pattern Anal. Mach. Intell.*, vol. 24, no. 1, pp. 90–102, Jan. 2002.

[31] L. Silva, O. R. P. Bellon, and K. L. Boyer, "Precision range image registration using a robust surface interpenetration measure and enhanced genetic algorithms," *IEEE Trans. Pattern Anal. Mach. Intell.*, vol. 27, no. 5, pp. 762–776, May 2005, doi: 10.1109/TPAMI.2005.108.

[32] B.-U. Lee, C.-M. Kim, and R.-H. Park, "An orientation reliability matrix for the iterative closest point algorithm," *IEEE Trans. Pattern Anal. Mach. Intell.*, vol. 22, no. 10, pp. 1205–1208, Oct. 2000.

[33] C. Zhang, S. Du, J. Liu, and J. Xue, "Robust 3D point set registration using iterative closest point algorithm with bounded rotation angle," *Signal Process.*, vol. 120, pp. 777–788, Mar. 2016.

[34] U. Bhattacharya and V. M. Govindu, "Efficient and robust registration on the 3D special Euclidean group," in *Proc. IEEE/CVF Int. Conf. Comput. Vis. (ICCV)*, Oct. 2019, pp. 5885–5894.

[35] V. M. Govindu, "Lie-algebraic averaging for globally consistent motion estimation," in *Proc. IEEE Comput. Soc. Conf. Comput. Vis. Pattern Recognit.*, Jul. 2004, pp. 684–691.

[36] H. Balta, J. Velagic, H. Beglerovic, G. De Cubber, and B. Siciliano, "3D registration and integrated segmentation framework for heterogeneous unmanned robotic systems," *Remote Sens.*, vol. 12, no. 10, p. 1608, May 2020.

[37] P. M. Knupp, "Algebraic mesh quality metrics," *SIAM J. Sci. Comput.*, vol. 23, no. 1, pp. 193–218, Jan. 2001.

[38] R. W. Sumner and J. Popović, "Deformation transfer for triangle meshes," *ACM Trans. Graph.*, vol. 23, no. 3, pp. 399–405, Aug. 2004.

[39] B. Amberg, S. Romdhani, and T. Vetter, "Optimal step nonrigid ICP algorithms for surface registration," in *Proc. IEEE Conf. Comput. Vis. Pattern Recognit.*, Jun. 2007, pp. 1–8.

[40] J. Süßmuth, M. Winter, and G. Greiner, "Reconstructing animated meshes from time-varying point clouds," *Comput. Graph. Forum*, vol. 27, no. 5, pp. 1469–1476, 2008.

[41] O. Sorkine and M. Alexa, "As-rigid-as-possible surface modeling," *Symp. Geometry Process.*, vol. 4, pp. 109–116, 2007.

[42] M. Liao, Q. Zhang, H. Wang, R. Yang, and M. Gong, "Modeling deformable objects from a single depth camera," in *Proc. IEEE 12th Int. Conf. Comput. Vis.*, Sep. 2009, pp. 167–174.

[43] H. Chui and A. Rangarajan, "A new point matching algorithm for non-rigid registration," *Comput. Vis. Image Understand.*, vol. 89, nos. 2–3, pp. 114–141, Feb. 2003.

[44] M. Rouhani, E. Boyer, and A. D. Sappa, "Non-rigid registration meets surface reconstruction," in *Proc. 2nd Int. Conf. 3D Vis.*, Dec. 2014, pp. 617–624.

[45] J. Yang, K. Li, K. Li, and Y.-K. Lai, "Sparse non-rigid registration of 3D shapes," *Comput. Graph. Forum*, vol. 34, no. 5, pp. 89–99, 2015.

[46] L. Xiong, L. Wu, W. Cui, S. Zhang, G. Xu, and H. Hu, "Robust non-rigid registration based on affine ICP algorithm and part-based method," *Neural Process. Lett.*, vol. 48, no. 3, pp. 1305–1321, Dec. 2018.

[47] L. Wu *et al.*, "Robust non-rigid registration algorithm based on local affine registration," in *Proc. 9th Int. Conf. Graphic Image Process. (ICGIP)*, Apr. 2018, pp. 920–927.

[48] M. L. Tazir, T. Gokhool, P. Checchin, L. Malaterre, and L. Trassoudaine, "CICP: Cluster Iterative closest point for sparse–dense point cloud registration," *Robot. Autom. Syst.*, vol. 108, pp. 66–86, Jan. 2018.

[49] A. Chaudhury, "Multilevel optimization for registration of deformable point clouds," *IEEE Trans. Image Process.*, vol. 29, pp. 8735–8746, 2020.

[50] Z. Xu and G. Xu, "Discrete schemes for Gaussian curvature and their convergence," *Comput. Math. Appl.*, vol. 57, no. 7, pp. 1187–1195, Apr. 2009.

[51] M. Dekker, *Mathematical Programming*, vol. 4. Boca Raton, FL, USA: CRC Press, 1986.

[52] H. K. Khalil and J. W. Grizzle, *Nonlinear System*, vol. 3. Upper Saddle River, NJ, USA: Prentice-Hall, 2002.

[53] F. Tajdari, N. E. Toulkani, and N. Zhilakzadeh, "Semi-real evaluation, and adaptive control of a 6DOF surgical robot," in *Proc. 11th Power Electron., Drive Syst., Technol. Conf. (PEDSTC)*, Feb. 2020, pp. 1–6.

[54] F. Tajdari, M. Tajdari, and A. Rezaei, "Discrete time delay feedback control of stewart platform with intelligent optimizer weight tuner," in *Proc. IEEE Int. Conf. Robot. Autom. (ICRA)*, May 2021, pp. 1–7.

[55] F. Tajdari, N. E. Toulkani, and N. Zhilakzadeh, "Intelligent optimal feed-back torque control of a 6DOF surgical rotary robot," in *Proc. 11th Power Electron., Drive Syst., Technol. Conf. (PEDSTC)*, Feb. 2020, pp. 1–6.

[56] D. Pickup *et al.*, "SHREC'14 track: Shape retrieval of non-rigid 3D human models," in *Proc. 7th Eurograph. Workshop 3D Object Retr.*, 2014, pp. 1–10.

[57] S. Valette, J. M. Chassery, and R. Prost, "Generic remeshing of 3D triangular meshes with metric-dependent discrete Voronoi diagrams," *IEEE Trans. Vis. Comput. Graphics*, vol. 14, no. 2, pp. 369–381, Mar. 2008.

[58] TUDelft. (2020). *DINED/Anthropometry Design*. [Online]. Available: https://dined.io.tudelft.nl/en

[59] (2018). *Artec Eva Fast 3D Scanner for Professionals*. [Online]. Available: https://www.artec3d.com/portable-3d-scanners/artec-eva

[60] H. Bennani, B. McCane, and J. Cornwall, "Three dimensional (3D) lumbar vertebrae data set," *Data Sci. J.*, vol. 15, pp. 1–15, Aug. 2016.

[61] K. M. Robinette, S. Blackwell, H. Daanen, M. Boehmer, and S. Fleming, "Civilian American and European surface anthropometry resource (caesar), final report. volume 1. summary," Sytronics, Beavercreek, OH, USA, Tech. Rep. ADA406704, 2002.

[62] Russian3Dscanner. (2019). *Wrap 3.4*. [Online]. Available: https://www.russian3dscanner.com/

[63] N. Charlie. (2020). *NRICP—Non-Rigid Iterative Closest Point*. [Online]. Available: https://www.mathworks.com/matlabcentral/fileexchange/54077-optimal-step-nonrigid-icp

[64] T. A. Davis, "Algorithm 832: UMFPACK V4. 3—An unsymmetric-pattern multifrontal method," *ACM Trans. Math. Softw.*, vol. 30, no. 2, pp. 196–199, 2004.

[65] S. C. Lee and M. Kazhdan, *Dense Point-to-Point Correspondences Between Genus-Zero Shapes*, vol. 38, no. 5. Hoboken, NJ, USA: Wiley, 2019, pp. 27–37.

[66] M. Vestner *et al.*, "Efficient deformable shape correspondence via kernel matching," in *Proc. Int. Conf. 3D Vis. (3DV)*, 2017, pp. 517–526.

[67] A. Myronenko and X. Song, "Point set registration: Coherent point drift," *IEEE Trans. Pattern Anal. Mach. Intell.*, vol. 32, no. 12, pp. 2262–2275, Dec. 2010.

[68] S. C. Lee and M. Kazhdan. (2019). *Executable Source Code*. [Online]. Available: https://github.com/mkazhdan/DenseP2PCorrespondences

[69] M. Vestner. (2017). *Executable Source Code*. [Online]. Available: https://github.com/zorah/KernelMatching

[70] A. Myronenko and X. Song. (2010). *Executable Source Code*. [Online]. Available: https://github.com/markeroon/CoherentPointDrift

[71] O. Hirose. (2010). *Executable Source Code*. [Online]. Available: https://github.com/ohirose/bcpd

[72] H. Dai, N. Pears, and W. Smith, "Non-rigid 3D shape registration using an adaptive template," in *Proc. Eur. Conf. Comput. Vis. (ECCV) Workshops*, 2018, pp. 48–63.

[73] X. Ge, "Non-rigid registration of 3D point clouds under isometric deformation," *ISPRS J. Photogramm. Remote Sens.*, vol. 121, pp. 192–202, Nov. 2016.

[74] V. G. Kim, Y. Lipman, and T. Funkhouser, "Blended intrinsic maps," *ACM Trans. Graph.*, vol. 30, no. 4, pp. 1–12, 2011.

[75] D. Luft and V. Schulz, "Pre-shape calculus: Foundations and application to mesh quality optimization," 2020, *arXiv:2012.09124*.

[76] X. Chen, J. Liu, Y. Pang, J. Chen, L. Chi, and C. Gong, "Developing a new mesh quality evaluation method based on convolutional neural network," *Eng. Appl. Comput. Fluid Mech.*, vol. 14, no. 1, pp. 391–400, Jan. 2020.

[77] L. A. Freitag, "On combining Laplacian and optimization-based mesh smoothing techniques," Argonne Nat. Lab., Lemont, IL, USA, Tech. Rep., 1997, pp. 37–43, vol. 220.

[78] P. L. George, "Tet meshing: Construction, optimization and adaptation," in *Proc. 8th Int. Meshing Roundtable*, 1999, pp. 133–141.

[79] R. Durand, B. Pantoja-Rosero, and V. Oliveira, "A general mesh smoothing method for finite elements," *Finite Elements Anal. Des.*, vol. 158, pp. 17–30, Oct. 2019.

[80] A. Liu and B. Joe, "Relationship between tetrahedron shape measures," *BIT Numer. Math.*, vol. 34, no. 2, pp. 268–287, Jun. 1994.

[81] F. Tajdari and N. Ebrahimi Toulkani, "Implementation and intelligent gain tuning feedback–based optimal torque control of a rotary parallel robot," *J. Vib. Control*, vol. 2012, May 2021, Art. no. 10775463211019177.

Farzam Tajdari received the master's degree in mechanical engineering from the Amirkabir University of Technology, Tehran, Iran, in 2016. He is currently pursuing the Ph.D. degree with the Faculty of Industrial Design Engineering, Delft University of Technology, The Netherlands. He is also working on 3D scanning and ergonomics. His research interests include pattern recognition, optimization, control theory, and non-linear systems.

Toon Huysmans received the Ph.D. degree from the Department of Physics, University of Antwerp, Belgium. He is currently working as an Assistant Professor of digital human modeling at the Faculty of Industrial Design Engineering, Delft University of Technology. His main research interests include anthropometric and bio-mechanical digital human modeling and simulation focus on data-driven methods and design tools in the fields of ergonomics, anatomy, and orthopaedics. He has a specific interest in the design of ultra-personalized products and services.

Yusheng Yang received the Ph.D. degree from the School of Mechatronic Engineering and Automation, Shanghai University, China. From 2018 to 2020, he studied at the Faculty of Industrial Design Engineering, Delft University of Technology, The Netherlands, as a Visiting Ph.D. Student. He is currently a Postdoctoral Researcher at Shanghai University. His main research interests include 3D scanning, human–robot interaction, and ergonomics.

Yu (Wolf) Song (Member, IEEE) received the Ph.D. degree from the Department of Mechanical Engineering, The University of Hong Kong. He joined the Faculty of Industrial Design Engineering, Delft University of Technology, in 2001. He is currently an Associate Professor with the Department of Sustainable Design Engineering. His main research interests include 3D scanning, 3D printed electronics, and ergonomics.